PCCP

ROYAL SOCIETY OF CHEMISTRY

PAPER

Cite this: DOI: 10.1039/d2cp02750j

$LiMn_2O_4$ cathodes with F anion doping for superior performance of lithium-ion batteries†

Zijing Wan, Xiaoxue Jiang, Dongwei Xu * and Xiaobing Luo

Although considered as promising candidates for lithium-ion secondary batteries, spinel $LiMn_2O_4$ cathodes suffer from significant capacity decay owing to the Jahn–Teller effect, dissolution of Mn and lattice oxygen loss during the charge/discharge process, preventing their wider use. In this work, we realize that F-doping at small concentrations could improve the battery voltage and reduce the capacity decay using an atomistic model. For voltage, F-doping improves the voltage to about 4.4 eV under large delithiation. For capacity decay, it retards capacity decay owing to the reduced lattice oxygen loss. The larger Gibbs free energy of oxygen release after F-doping indicates harder lattice oxygen loss. In addition, although F-doping makes the average valence of Mn lower, the existence of Mn^{4+} during delithiation exerts a positive effect by reducing the Jahn–Teller effect. However, since the Mn^{3+} ions in the spinel structure could induce Jahn–Teller distortion, the effect of F-doping on Jahn–Teller distortion is determined by the competition between Mn^{4+} and Mn^{3+}. The atomistic mechanism of F-doping in the performance of $LiMn_2O_4$ offers new insight in developing spinel lithium manganese oxide cathode materials with superior performance.

Received 17th June 2022,
Accepted 24th August 2022

DOI: 10.1039/d2cp02750j

rsc.li/pccp

1 Introduction

Energy security and storage technologies are key strategic concerns related to national economies and the development of societies.[1–3] To step out of environmental dilemmas and satisfy energy demands, a new energy technology named lithium-ion secondary batteries (LIBs) with excellent safety performance and high energy density is born, which has succeeded in portable electronic products, electric vehicles and even large energy storage systems.[4–6] Furthermore, the electrochemical performance of LIBs, such as the output voltage, energy density and structural stability, is dramatically determined by the cathode materials.[7–9]

Up to now, spinel $LiMn_2O_4$ (LMO) cathodes have been considered as promising candidates owing to their high energy density, low cost, environment-friendly nature, three-dimensional diffusion channels of Li^+, *etc.*[10,11] However, spinel LMO suffers from inferior voltage[12] and significant capacity decay[13] during cycling, preventing its wider use. The significant capacity decay is mainly due to the Jahn–Teller effect associated with Mn^{3+} ions[14,15] shown in Fig. 1, dissolution of Mn associated with Mn^{2+} ions[16,17] and irreversible lattice oxygen loss,[18–20] which is related to the stability of the LMO material. From an atomic point of view, the oxygen ions become more reductive and lose electrons to form oxygen, resulting in inevitable capacity decay and greater charge transfer resistance.

Many studies on the modification of LMO-based LIBs have been extensively carried out to enhance their performance. General modification schemes include guest element substitution, surface coating, and morphology regulation. Compared with the other two modification investigations, element substitution undoubtedly appears to be a more favorable strategy owing to strengthening the crystallographic structure of spinel LMO, reducing the Li^+ transport barrier and increasing the ion transport rate.[21] Consequently, substituting a small fraction of LMO with several ions such as Al,[22] Ni,[23] Ti,[24] Fe,[25] Cr,[26] Mg,[27] Zn,[28] S,[29] Cl,[30] Br,[31] and F[32] has been attempted to enhance the performance of LMO-based LIBs. Compared with cation doping, anion doping avoids the undesirable occupation of Li and effectively contributes to the redox activity of Mn, both of which are critical for the battery performance.[33] Furthermore, spinel $Li_{1.68}Mn_{1.6}O_4$,[32] $Li_{1.6}Mn_{1.6}O_4$[34] and $LiMn_2O_4$[35] cathodes doped with F anions display ultrahigh power and energy density in experiments, which reveals the strategy of F-doping is practicable. However, only at small concentrations, F-doping has satisfactory performance. When excessive F ions are doped, battery voltage decreases and capacity decay intensifies.[34,35] However, the mechanism of F-doping at small concentrations on spinel lithium manganese oxide lacks further research.

State Key Laboratory of Coal Combustion, School of Energy and Power Engineering, Huazhong University of Science and Technology, Wuhan, Hubei 430074, China. E-mail: dwxu@hust.edu.cn

† Electronic supplementary information (ESI) available: Details of the optimized structure of $Li_xMn_2O_4$, PDOS of different Mn atoms, and the ball and stick model of the Mn3–O octahedron during delithiation (x = 1, 0.75, 0.5, 0.25 and 0). See DOI: https://doi.org/10.1039/d2cp02750j

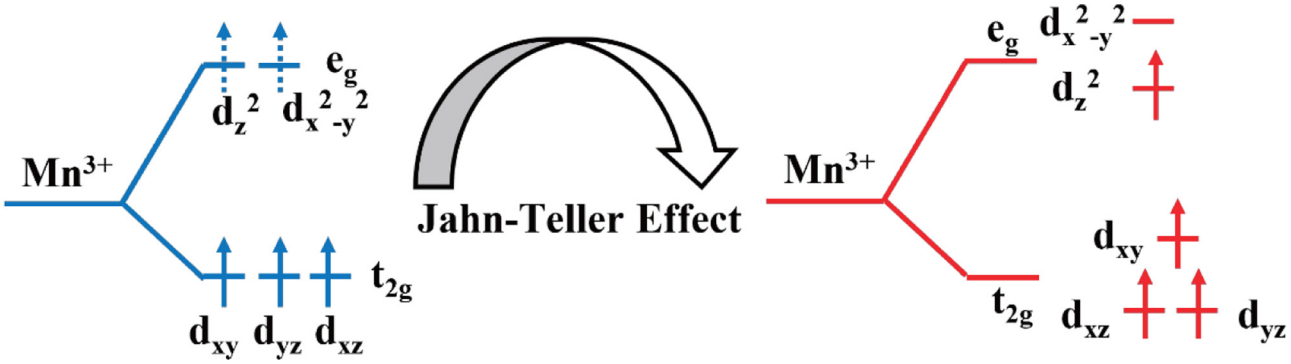

Fig. 1 Schematic illustration of the Jahn–Teller effect with Mn^{3+} ions at the octahedral site. Note that the dotted arrows represent candidate orbitals the electrons could occupy.

In this work, we report the effect of F-doping on spinel LMO by using density functional theory (DFT) with van der Waals correction. For comparison, the properties including the voltage and capacity decay of $Li_xMn_2O_{3.875}F_{0.125}$ (LMOF) and $Li_xMn_2O_4$, in which reversible de-intercalation/intercalation of lithium occurs around 4 V,[36] are calculated with x = 0, 0.25, 0.5, 0.75, 1. Our results reveal the desirable effect of F-doping on spinel LMO, explaining the experimental observations. Furthermore, it may offer insight into improving battery performance by halogenated element doping on spinel lithium manganese oxide cathode materials.

2 Computational details

All spin-polarized density functional theory calculations are performed using the Vienna *Ab initio* Simulation Package (VASP 6.1.0).[37,38] Projector augmented wave pseudopotentials are used to model the core electrons[39] by treating the Li 2s 2p and Mn 3d 4s electrons as valence electrons, respectively. The generalized gradient approximation (GGA) of Perdew–Burke–Ernzerhof (PBE) is selected to describe the exchange-correlation of valence electrons.[40] The Brillouin zone is sampled with a size-dependent Γ-point-centered k-point mesh of 4 × 4 × 4 size. Gaussian smearing with a width of 0.05 eV and an energy cutoff of 520 eV for the plane wave representation are used for calculations. Geometry optimizations are conducted *via* the quasi-Newton method. All atoms in the bulk calculations are subjected to full ionic relaxation and converged to an energy tolerance of 0.1 meV and a force criterion of 0.02 eV $Å^{-1}$.[41] To correctly investigate the properties of transition metal oxides, a Hubbard correction[42] applied to 3d orbitals to improve the description of the electron localization is a good approximation. The effective Hubbard U for Mn element we used in the GGA+U[43] calculations is 3.5 eV.[44] The initial magnetic moments for the Mn atoms are set to be 3.5 μ_B $atom^{-1}$ [45] with ferromagnetic ordering and the whole cubic structure is allowed to relax during the simulations. In addition, the DFT+D3 method for the modeling of the long-range dispersion interactions[46] is also included in all calculations. In this work, we use a supercell composed of eight-formula units of cubic LMO, which is the $Fd\bar{3}m$ space group (No. 227)[47] shown in Fig. 2. According to the principle of minimum energy, the F-doping structure ($LiMn_2O_{3.875}F_{0.125}$) is chosen out of total ten structures considering the symmetry of the space group in Fig. 2. Fig. 2 also shows the optimal lithium ion distributions in delithiated structures of ($Li_xMn_2O_{3.875}F_{0.125}$) ($x$ = 0.75, 0.5, 0.25 and 0), which are selected from 28, 15, 6, and 1 candidate structures, respectively. To compare, the full process of delithiation in $Li_xMn_2O_4$ with x = 1, 0.75, 0.5, 0.25, 0 is also shown in Fig. 2. The number '10' and C_m^n next to the arrows in the figure represent the total possible structures during doping and delithiation processes, where m and n represent the total different Li sites and the number of possible delithiated Li ions, respectively, considering the symmetry.

3 Results and discussion

3.1 Redox potential

The output voltage of LIBs is related to the redox potential of the cathode and anode.[33] The redox potential represents the energy effort taken to extract the lithium ions from the electrode. The optimized voltage of cathode materials should be more than 3.5 V, since potentials below 3.5 V would aggravate the delivered energy density. In this work, the effect of F-doping on the output voltage is assessed using the following formula:

$$V = -\frac{E(LiMn_2O_4) - (1-x)\cdot E(Li) - E(Li_xMn_2O_4)}{x\cdot e} \quad (1)$$

where $E(LiMn_2O_4)$, $E(Li)$, and $E(Li_xMn_2O_4)$ are the calculated total energies with the lithiated spinel structure, bulk BCC Li metal,[50] and delithiated spinel structure by the DFT+D3 method, respectively. Based on previous experimental observations and theoretical predictions, the charging/discharging process can be approximately divided into four stages with five stable structures ($Li_xMn_2O_4$) at x = 0, 0.25, 0.5, 0.75, 1.[51] The whole calculated charging profiles of pristine and F-doped LMO are illustrated in Fig. 3, where the experimental charging profile of pristine LMO is also given by hollow triangles for comparison. Notably, our result about the charging profile of pristine LMO is consistent with the experiment within a five percent margin of error. In the first delithiation stage ($0.75 \le x \le 1$), F-

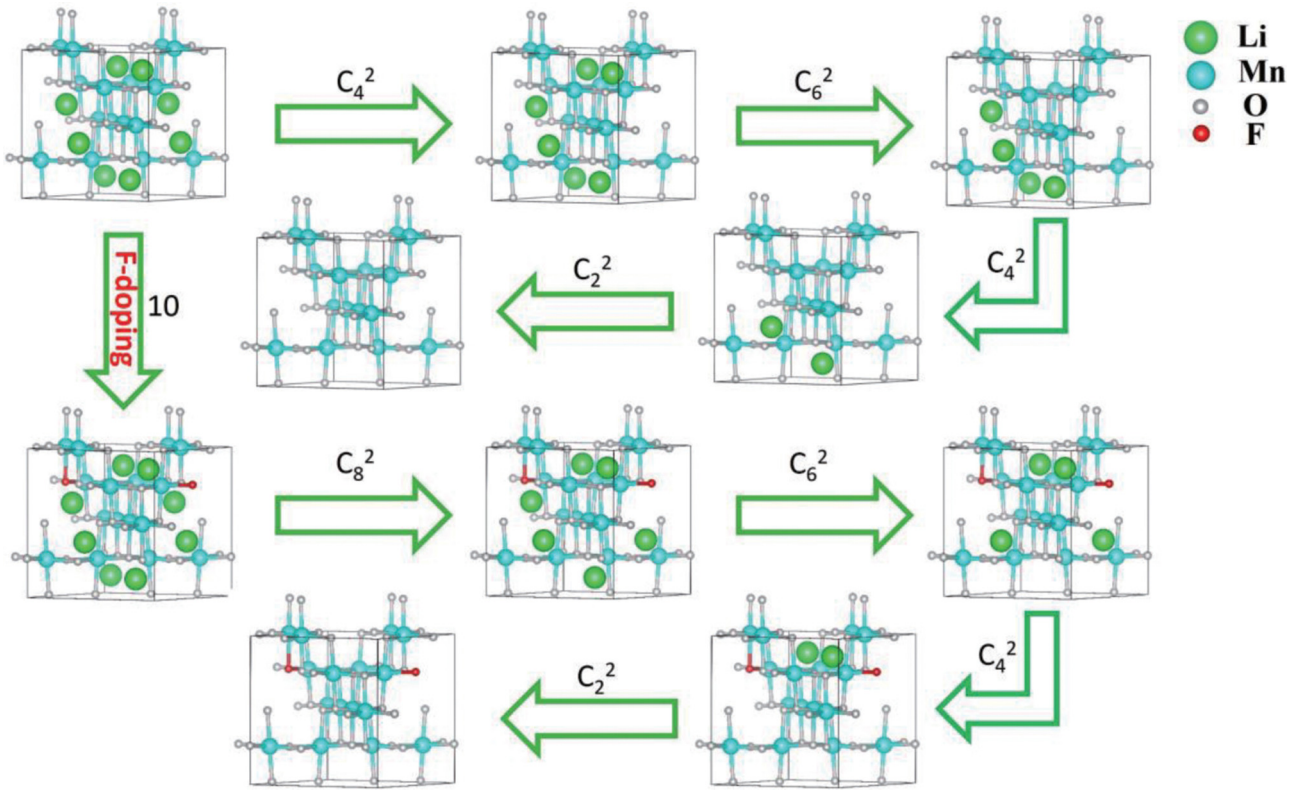

Fig. 2 Schematic illustration of the delithiation process in LMO and LMOF. Note each step involves the removal of two lithium ions from the previous structure. Green spheres are Li, cyan spheres are Mn, grey spheres are O, and red spheres are F.

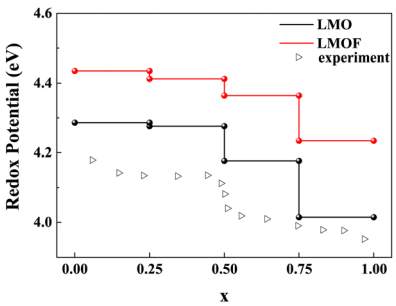

Fig. 3 Charging profiles of pristine and F-doping LMO. Note the data of LMO are obtained in experiments.[48,49]

doping increases the redox potential by 0.22 eV, demonstrating the positive effect of F-doping on voltage. At the stage of $0.5 \leq x \leq 0.75$, the redox potential of LMOF suddenly increases by 0.13 eV compared with the first stage, which is consistent with the voltage jump of pristine LMO at $x = 0.75$. In the third ($0.25 \leq x \leq 0.5$) and last stages ($0 \leq x \leq 0.25$), the redox potential of LMOF changes slightly, showing good consistency with the pristine LMO. In all, F-doping could improve the voltage more than 0.1 eV compared with the pristine LMO during the whole delithiation process according to the simulated charging profile. These calculations agree with experimental reports which demonstrate that F-doping at a concentration of 0.2 improves the voltage compared with pristine LMO.[35]

3.2 Capacity decay

The capacity decay is related to the Jahn–Teller effect induced distortion and the dissolution of Mn, which are both related to the valence change of Mn ions by analysing Bader charges and projected density of states. In addition, it is also related to the difficulty level of lattice oxygen loss by calculating the Gibbs free energy.

3.2.1 Bader charges. To reveal the charge transfer of the Mn ions in $Li_xMn_2O_{3.875}F_{0.125}$ at $x = 1$, 0.75, 0.5, 0.25, 0, the Bader charge[52] is calculated for the delithiation intermediates in Fig. 4(b). Note that the Bader charge could be normally underestimated.[44,53] The Mn ions could be classified into three types, two types of them (higher charge Mn1 and Mn4 and lower charge Mn2) staying away from doping F anions and the other type (Mn3) next to the F anion in LMOF. To visualize them more clearly, their locations are shown in Fig. 4(a). After doping, the charge difference of the three types of Mn ions becomes significant. Mn1 shows relatively high charge compared with Mn2 and Mn3 during the whole delithiation process before desorbing all the Li ions. In addition, sensibility to the delithiation is different for the three types of Mn ions for LMOF. The maximum charge reduction of the Mn1 (Mn4) ion is 0.05 (0.06) e^- in the whole delithiation process, indicating low electrochemical activity during cycle. For the Mn3 ion, the charge fluctuates considerably and the maximum charge reduction is about 0.40 e^- during delithiation. Different from the charge-transfer of Mn ions, the oxygen anionic redox in

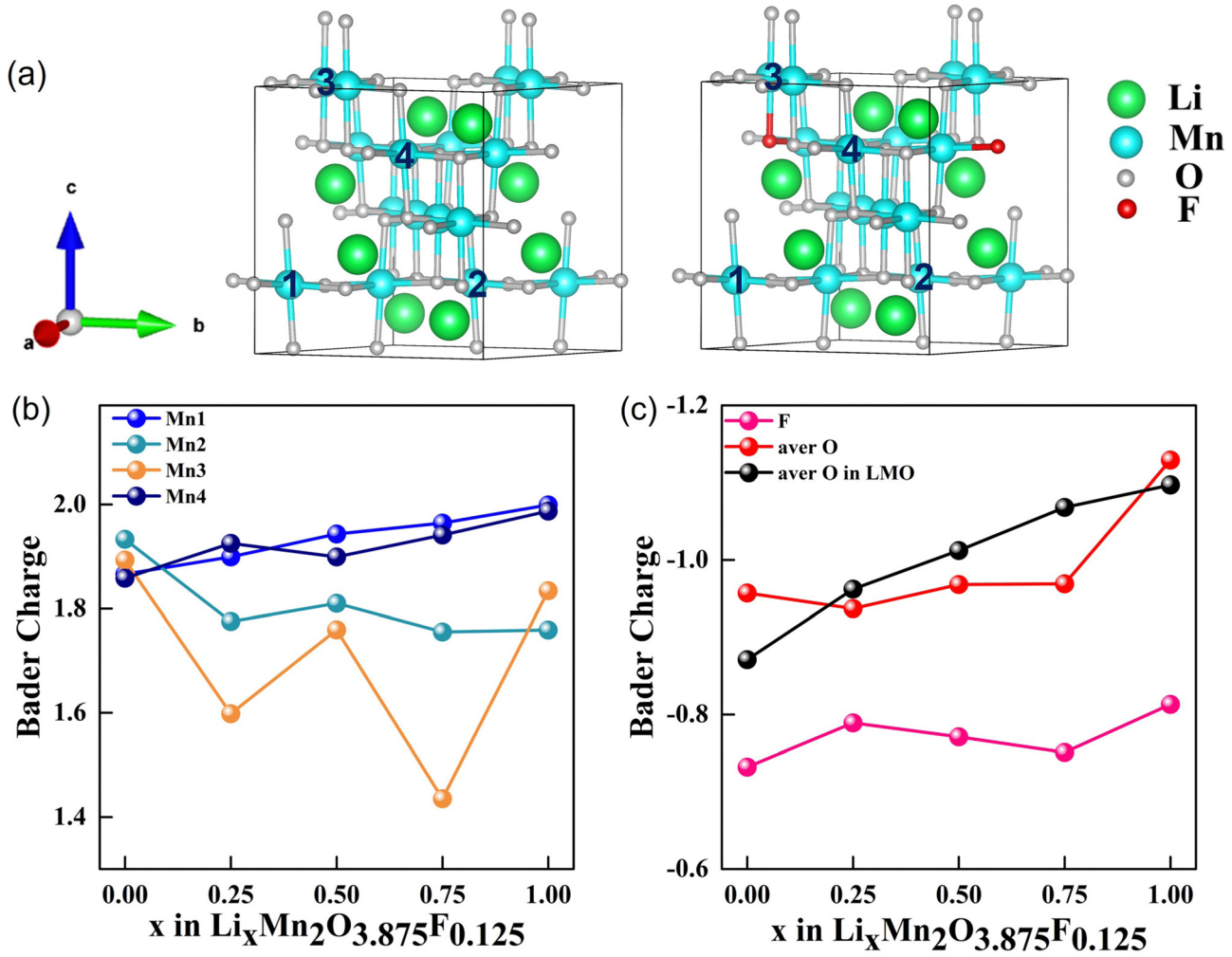

Fig. 4 (a) The positions of Mn1, Mn2, Mn3, and Mn4 in the $Li_xMn_2O_4$ and $Li_xMn_2O_{3.875}F_{0.125}$ structures. Note the number denotes the type of Mn. Calculated Bader charges of (b) Mn1, Mn2, Mn3 and Mn4, and (c) the F and average O atom of the ground state structure of $Li_xMn_2O_{3.875}F_{0.125}$ in the delithiation process (x = 1, 0.75, 0.5, 0.25 and 0). For comparison, the calculated Bader charge of the average O atom in $Li_xMn_2O_4$ is also given in (c).

both LMO and LMOF remains electrochemically active during delithiation based on the Bader charge calculations in Fig. 4(c). In fact, anion doping is favorable in reducing oxygen participation for electrochemical redox. During the whole delithiation process, the average charge of O atoms in LMOF only reduces 0.17 e^- in total, while that in pristine LMO reduces 0.23 e^-, indicating that F-doping effectively suppresses the reduction of the average charge of the O atoms.

3.2.2 Projected density of states. As mentioned above, electron transfer of the Mn-3d orbitals (valence) plays a vital role in determining the Jahn–Teller effect and the dissolution of Mn. To further reveal the charge transfer during delithiation, the projected density of states (PDOS) of all 3d orbitals of Mn1, Mn2, Mn3, and Mn4 ions in $Li_xMn_2O_{3.875}F_{0.125}$ (x = 1, 0.75, 0.5, 0.25, 0) and $Li_xMn_2O_4$ (x = 1, 0.75, 0.5, 0.25, 0) are illustrated in Fig. 5 and Fig. S1–S6 (ESI†). Fig. 5(a–c) and Fig. S1 (ESI†) show that the Mn1–t_{2g} orbitals in LMOF are fully occupied, while the Mn1–e_g orbitals are almost unoccupied during the whole delithiation process, indicating that the Mn1 ion is positive tetravalent. The tetravalent Mn1 ions after F-doping suppress the Jahn–Teller effect compared with the Mn1 ions in pristine LMO as shown in Fig. 5(d–f). In fact, we find two positive tetravalent ions (Mn1 and Mn4) by checking the PDOS and Bader charges of all Mn ions during delithiation. Furthermore, the electron occupation of the Mn4 ion is consistent with Mn1 in Fig. S6 (ESI†). For Mn2 ions, the charge variation with delithiation exhibits a similar trend for spinel LMO and LMOF as shown in Fig. S2 and S4 (ESI†), indicating the lower effect of F-doping on Mn2 ions. As for Mn3 ions neighboring the F ions, the situation is different as shown in Fig. S3 and S5 (ESI†). After F-doping, the Mn3–e_g orbitals are split and one electron in the Mn3 ion occupies the d_{z^2} orbital during delithiation, indicating the positive trivalent nature of the Mn3 ion. This leads to stretching of the Mn-O octahedra along the c-axis as shown in Fig. S7 (ESI†). To describe the distribution of transition metal oxides, the distortion index introduced by Baur[54,55] is employed:

$$\mathrm{JTI} = \frac{1}{n}\sum_{i=1}^{n}\frac{|l_i - l_{\mathrm{av}}|}{l_{\mathrm{av}}} \quad (2)$$

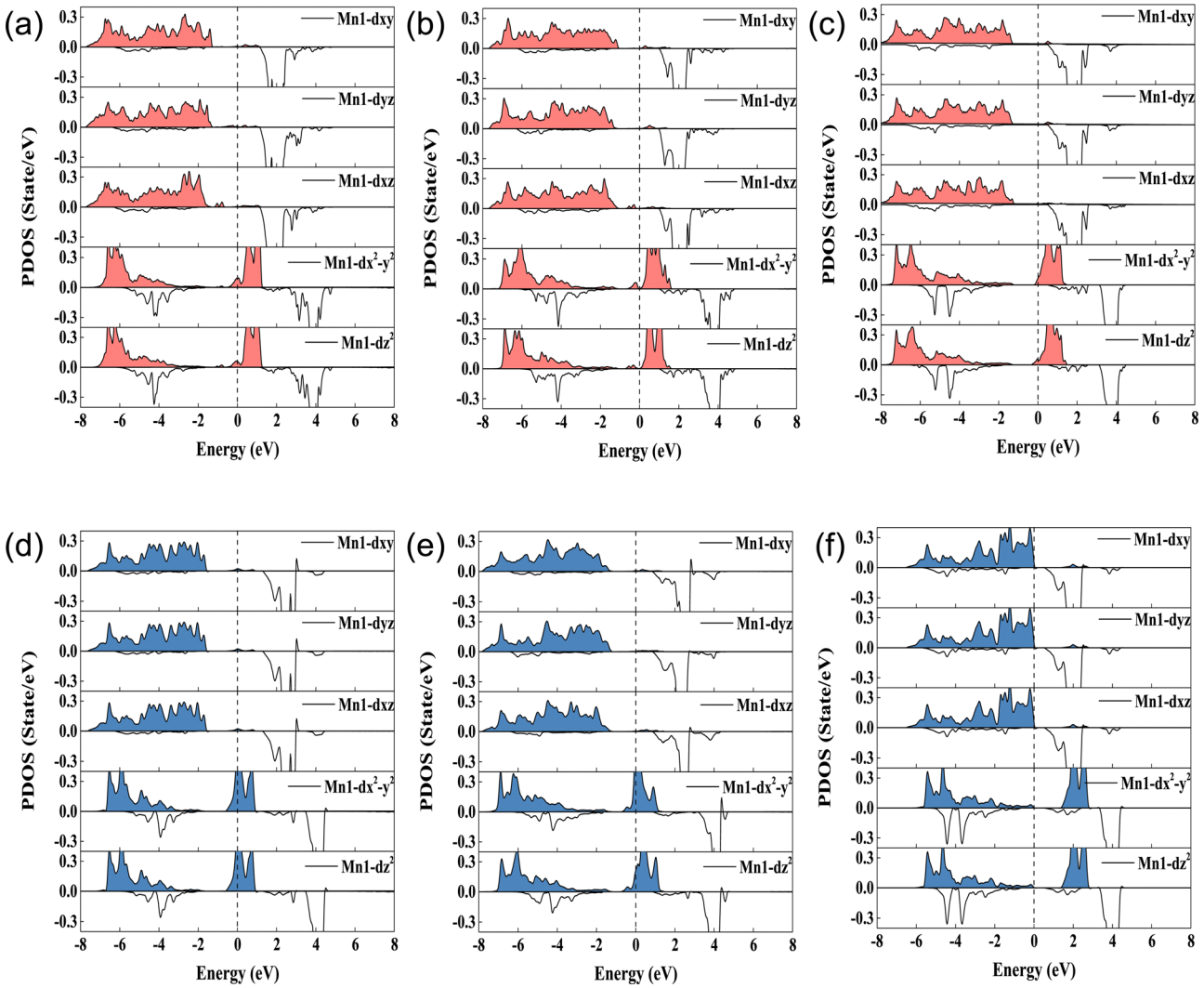

Fig. 5 PDOS of five Mn1-3d orbitals in (a–c) $Li_xMn_2O_{3.875}F_{0.125}$ and (d–f) $Li_xMn_2O_4$ in the delithiation process (x = 1, 0.5, 0). The shaded area and blank stand for the majority and minority channels of the spins, respectively.

where n is the number of bonds of the transition metal, l_i is the length of a bond in the 'i' direction, and l_{av} is the average length of all bonds. In Table 1, the maximum JTI values of Mn3 and Mn1 (Mn4) ions in $Li_{0.75}Mn_2O_{3.875}F_{0.125}$ are 0.048 and 0.013 (0.012) respectively, with the relative magnitude being consistent with the analysis of PDOS. In all, when F anions are doped, Mn1 (Mn^{4+}) and Mn4 (Mn^{4+}) ions have a positive influence on the Jahn–Teller effect at the four stages of delithiation, while Mn3 (Mn^{3+}) ions have a negative influence on the Jahn–Teller effect. So the influence of F-doping on the Jahn–Teller effect is determined by the competition between Mn^{3+} and Mn^{4+} ions. On the other hand, no divalent Mn ion is present during delithiation, indicating that F-doping has little effect on the dissolution of Mn.

Table 1 The calculated JTI of Mn1, Mn2 and Mn3 in $Li_xMn_2O_{3.875}F_{0.125}$ with x = 0, 0.25, 0.5, 0.75, 1

	x = 1.00	x = 0.75	x = 0.50	x = 0.25	x = 0.00
Mn1	0.012	0.012	0.007	0.013	0.005
Mn2	0.048	0.048	0.048	0.017	0.002
Mn3	0.046	0.048	0.037	0.037	0.023
Mn4	0.012	0.010	0.008	0.007	0.005

3.2.3 Gibbs free energy of oxygen release. To reveal the doping effect of F ions on lattice oxygen loss, a criterion is to determine the O atomic redox process, which could correspond to the level of oxygen release. According to previous studies in experiments[56] and theories,[57] the O atoms break bonds with neighbouring atoms (Mn–O, Li–O) and lose electrons, leading to the formation of an O–O bond and the release of oxygen. Both thermodynamic and kinetic factors must be taken into account in the oxygen release. Therefore, the Gibbs free energy (ΔG) of oxygen release is widely acknowledged as the most satisfying criterion to determine the ease of oxygen release.[58,59] The oxygen release could be described as follows:

$$Li_xMn_2O_4 = Li_xMn_2O_{4-z} + z/2O_2 \quad (3)$$

where z is the amount of O atoms removed from the spinel LMO. We assume that $Li_xMn_2O_{4-z}$ is obtained by removing the

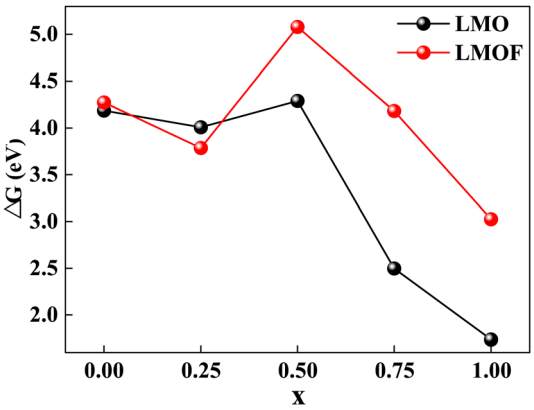

Fig. 6 The calculated Gibbs free energy for O_2 release in $Li_xMn_2O_4$ and $Li_xMn_2O_{3.875}F_{0.125}$ with x = 0, 0.25, 0.5, 0.75, 1.

lowest Bader charge O atom. Hence, the Gibbs free energy can be described as follows:

$$\Delta G = \frac{1}{0.5z} \times [E(Li_xMn_2O_{4-z}) + 0.5zE(O_2) - E(Li_xMn_2O_4)] - T\Delta S(O_2) \quad (4)$$

where $E(Li_xMn_2O_{4-z})$ and $E(Li_xMn_2O_4)$ are the calculated energies with delithiated states before and after O_2 released states using the DFT+D3 method, respectively. The energy of O_2 is calculated to be −9.935 eV, which is consistent with Liu's result (−9.87 eV).[60] Taking into account the entropy of O_2 at the standard state ($T\Delta S$ = 0.63 eV),[61] the Gibbs free energy ΔG can be calculated based on the above reaction formula as shown in Fig. 6. Notably, the Gibbs free energy ΔG in LMOF is almost always higher than that in LMO during the delithiated cycle, indicating that releasing oxygen from LMOF is more difficult than from pristine LMO. The difference between the Gibbs free energy ΔG in LMO and that in LMOF reaches a maximum of 1.686 eV at x = 0.75. Remarkably, the Gibbs free energy ΔG in LMOF reaches a maximum of 5.08 eV at x = 0.5, at which the oxygen release is difficult to occur in $Li_{0.5}Mn_2O_{3.875}F_{0.125}$. In short, F-doping can reduce the difficulty level of oxygen loss and retard capacity decay.

4 Conclusions

In summary, a small amount (1/32) of F-doping on LMO spinel has positive effects on improving the voltage and suppressing the capacity decay, which could be applied in LIBs for superior performance. For voltage, the calculated and experimental voltages of LMO are within a five percent difference and we find F-doping can improve the voltage to about 4.4 eV at large delithiation. In the case of lattice oxygen release, the Gibbs free energy ΔG in LMOF is almost always higher compared with LMO, demonstrating F-doping could reduce the difficulty level of oxygen loss and retard capacity decay. Although F-doping makes the average valence of Mn lower, the existence of Mn^{4+} far away from doping F ions plays a positive role in reducing the Jahn–Teller effect. However, owing to the existence of Mn^{3+}, whether F-doping can reduce the Jahn–Teller effect is determined by the competition between by Mn^{3+} and Mn^{4+} ions. Our work on F-doping at small concentrations may shed light on the future development of anion doping based on spinel lithium manganese.

Conflicts of interest

There are no conflicts to declare.

Acknowledgements

D. X. acknowledges the support from the National Natural Science Foundation of China (No. 51806072). Some of the computation was performed using the Tianhe II supercomputer in the National Super-computing Center at Guangzhou.

Notes and references

1 H. Hafiz, K. Suzuki, B. Barbiellini, N. Tsuji, N. Yabuuchi, K. Yamamoto, Y. Orikasa, Y. Uchimoto, Y. Sakurai and H. Sakurai, *et al.*, *Nature*, 2021, **594**, 213–216.
2 R. Wang, X. Chen, Z. Huang, J. Yang, F. Liu, M. Chu, T. Liu, C. Wang, W. Zhu and S. Li, *et al.*, *Nat. Commun.*, 2021, **12**, 1–10.
3 Y. Bi, J. Tao, Y. Wu, L. Li, Y. Xu, E. Hu, B. Wu, J. Hu, C. Wang and J.-G. Zhang, *et al.*, *Science*, 2020, **370**, 1313–1317.
4 Z. Luo, S. Li, L. Yang, Y. Tian, L. Xu, G. Zou, H. Hou, W. Wei, L. Chen and X. Ji, *Nano Energy*, 2021, **87**, 106212.
5 F. Wu, J. Maier and Y. Yu, *Chem. Soc. Rev.*, 2020, **49**, 1569–1614.
6 L. Yang, W. Deng, W. Xu, Y. Tian, A. Wang, B. Wang, G. Zou, H. Hou, W. Deng and X. Ji, *J. Mater. Chem. A*, 2021, **9**, 14214–14232.
7 J. Chen, W. Deng, X. Gao, S. Yin, L. Yang, H. Liu, G. Zou, H. Hou and X. Ji, *ACS Nano*, 2021, **15**, 6061–6104.
8 S. Yin, W. Deng, J. Chen, X. Gao, G. Zou, H. Hou and X. Ji, *Nano Energy*, 2021, **83**, 105854.
9 M. Li, J. Lu, Z. Chen and K. Amine, *Adv. Mater.*, 2018, **30**, 1800561.
10 M. M. Thackeray and K. Amine, *Nat. Energy*, 2021, **6**, 566.
11 Y. Huang, Y. Dong, S. Li, J. Lee, C. Wang, Z. Zhu, W. Xue, Y. Li and J. Li, *Adv. Energy Mater.*, 2021, **11**, 2000997.
12 F. Luo, C. Wei, C. Zhang, H. Gao, J. Niu, W. Ma, Z. Peng, Y. Bai and Z. Zhang, *J. Energy Chem.*, 2020, **44**, 138–146.
13 C. Zhan, T. Wu, J. Lu and K. Amine, *Energy Environ. Sci.*, 2018, **11**, 243–257.
14 K. I. Kugel and D. Khomski, *Phys.-Usp.*, 1982, **25**, 231.
15 C. Zuo, Z. Hu, R. Qi, J. Liu, Z. Li, J. Lu, C. Dong, K. Yang, W. Huang and C. Chen, *et al.*, *Adv. Eng. Mater.*, 2020, **10**, 2000363.
16 K. Leung, *Chem. Mater.*, 2017, **29**, 2550–2562.
17 H. Zheng, Q. Sun, G. Liu, X. Song and V. S. Battaglia, *J. Power Sources*, 2012, **207**, 134–140.

18 X. Hao, X. Lin, W. Lu and B. M. Bartlett, *ACS Appl. Mater. Interfaces*, 2014, **6**, 10849–10857.
19 W. Xu, Y. Zheng, L. Lin, W. Lei, Z. Wang, H. Song, Y. Cheng, R. Qi, H. Peng and H. Lin, *et al.*, *J. Alloys Compd.*, 2021, **870**, 159387.
20 X. Gao, Y. H. Ikuhara, C. A. Fisher, R. Huang, A. Kuwabara, H. Moriwake, K. Kohama and Y. Ikuhara, *J. Mater. Chem. A*, 2019, **7**, 8845–8854.
21 S. Zhang, W. Deng, R. Momen, S. Yin, J. Chen, A. Massoudi, G. Zou, H. Hou, W. Deng and X. Ji, *J. Mater. Chem. A*, 2021, **9**, 21532–21550.
22 Q. Liang, Z. Wang, W. Bai, J. Guo, M. Xiang, X. Liu and H. Bai, *J. Energy Storage*, 2021, **50**, 17052–17061.
23 Q. Liu, Q. Liang, J. Guo, M. Xiang, W. Bai, H. Bai and X. Liu, *Ceram. Int.*, 2021, **47**, 2441–2449.
24 J. Xue, H. Zhang, T. Yang and X. Zhang, *Int. J. Electrochem. Sci.*, 2020, **15**, 8732–8742.
25 H. Liu, R. Tian, Y. Jiang, X. Tan, J. Chen, L. Zhang, Y. Guo, H. Wang, L. Sun and W. Chu, *Electrochim. Acta*, 2015, **180**, 138–146.
26 J. Jiang, W. Li, H. Deng, G. Gong and N. Li, *J. Nanosci. Nanotechnol.*, 2019, **19**, 125–129.
27 H. Xu, Y. Chen, Y. Li, L. Kong, H. Li, C. Xu, Q. Su and M. Ren, *J. Solid State Electrochem.*, 2018, **22**, 3735–3742.
28 J.-Y. Piao, S.-Y. Duan, X.-J. Lin, X.-S. Tao, Y.-S. Xu, A.-M. Cao and L.-J. Wan, *Chem. Commun.*, 2018, **54**, 5326–5329.
29 Q. Jiang, D. Liu, H. Zhang and S. Wang, *J. Phys. Chem. C*, 2015, **119**, 28776–28782.
30 D.-W. Han, W.-H. Ryu, W.-K. Kim, J.-Y. Eom and H.-S. Kwon, *J. Phys. Chem. C*, 2013, **117**, 4913–4919.
31 Z. Dong, Y. Huang, D. Jia and Z. Guo, *J. Solid State Electrochem.*, 2011, **15**, 725–730.
32 H. Ji, J. Wu, Z. Cai, J. Liu, D.-H. Kwon, H. Kim, A. Urban, J. K. Papp, E. Foley and Y. Tian, *et al.*, *Nat. Energy*, 2020, **5**, 213–221.
33 F. Kong, C. Liang, R. C. Longo, D.-H. Yeon, Y. Zheng, J.-H. Park, S.-G. Doo and K. Cho, *Chem. Mater.*, 2016, **28**, 6942–6952.
34 F. Qian, B. Zhao, M. Guo, Z. Qian, Z. Wu and Z. Liu, *Mater. Des.*, 2020, **194**, 108867.
35 J. Son and H. G. Kim, *J. Power Sources*, 2005, **147**, 220–226.
36 Y. Jeon, H. K. Noh and H.-K. Song, *Sci. Rep.*, 2017, **7**, 1–9.
37 G. Kresse, J. Furthmüller and J. Hafner, *Phys. Rev. B: Condens. Matter Mater. Phys.*, 1994, **50**, 13181.
38 G. Kresse and J. Furthmüller, *Phys. Rev. B: Condens. Matter Mater. Phys.*, 1996, **54**, 11169.
39 G. Kresse and D. Joubert, *Phys. Rev. B: Condens. Matter Mater. Phys.*, 1999, **59**, 1758.
40 J. P. Perdew, K. Burke and M. Ernzerhof, *Phys. Rev. Lett.*, 1996, **77**, 3865.
41 D. Tang, Y. Sun, Z. Yang, L. Ben, L. Gu and X. Huang, *Chem. Mater.*, 2014, **26**, 3535–3543.
42 S. Dudarev, G. Botton, S. Savrasov, C. Humphreys and A. Sutton, *Phys. Rev. B: Condens. Matter Mater. Phys.*, 1998, **57**, 1505.
43 A. Peles, *J. Mater. Sci.*, 2012, **47**, 7542–7548.
44 D. Santos-Carballal, A. Roldan, R. Grau-Crespo and N. H. de Leeuw, *Phys. Rev. B: Condens. Matter Mater. Phys.*, 2015, **91**, 195106.
45 C. Ouyang, S. Shi and M. Lei, *J. Alloys Compd.*, 2009, **474**, 370–374.
46 S. Grimme, J. Antony, S. Ehrlich and H. Krieg, *J. Chem. Phys.*, 2010, **132**, 154104.
47 P. Strobel, G. Rousse, A. Ibarra-Palos and C. Masquelier, *J. Solid State Chem.*, 2004, **177**, 1–5.
48 J.-S. Kim, J. Prakash and J. Selman, *Electrochem. Solid-State Lett.*, 2001, **4**, A141.
49 H. Abiko, M. Hibino and T. Kudo, *Electrochem. Solid-State Lett.*, 1998, **1**, 114.
50 A. Raju Natarajan and A. Van der Ven, *Chem. Mater.*, 2019, **31**, 8222–8229.
51 M. A. Y. de Dompablo, A. Van der Ven and G. Ceder, *Phys. Rev. B: Condens. Matter Mater. Phys.*, 2002, **66**, 064112.
52 W. Tang, E. Sanville and G. Henkelman, *J. Phys.: Condens. Matter*, 2009, **21**, 084204.
53 A. Roldan, D. Santos-Carballal and N. H. de Leeuw, *J. Chem. Phys.*, 2013, **138**, 204712.
54 W. Baur, *Acta Crystallogr., Sect. B: Struct. Crystallogr. Cryst. Chem.*, 1974, **30**, 1195–1215.
55 H. Yang, C. N. Savory, B. J. Morgan, D. O. Scanlon, J. M. Skelton and A. Walsh, *Chem. Mater.*, 2020, **32**, 7542–7550.
56 A. R. Armstrong, M. Holzapfel, P. Novák, C. S. Johnson, S.-H. Kang, M. M. Thackeray and P. G. Bruce, *J. Am. Chem. Soc.*, 2006, **128**, 8694–8698.
57 R. Xiao, H. Li and L. Chen, *Chem. Mater.*, 2012, **24**, 4242–4251.
58 Y. Li, X. Zhao, Q. Bao, M. Cui, W. Qiu and J. Liu, *Energy Stor. Mater.*, 2020, **32**, 253–260.
59 B. Li, R. Shao, H. Yan, L. An, B. Zhang, H. Wei, J. Ma, D. Xia and X. Han, *Adv. Funct. Mater.*, 2016, **26**, 1330–1337.
60 E. Song, Y. Hu, R. Ma, Y. Li, X. Zhao, J. Wang and J. Liu, *J. Mater. Chem. A*, 2021, **9**, 9337–9346.
61 J. Hummelshøj, J. Blomqvist, S. Datta, T. Vegge, J. Rossmeisl, K. S. Thygesen, A. Luntz, K. W. Jacobsen and J. K. Nørskov, *J. Chem. Phys.*, 2010, **132**, 071101.